Irons, L.; Latorre, M.; Humphrey, JD. (2021). From Transcript to Tissue: Multiscale Modeling from Cell Signaling to Matrix Remodeling. Annals of Biomedical Engineering. 48(7):1701-1715. https://doi.org/10.1007/s10439-020-02713-8

From Transcript to Tissue: Multiscale Modeling from Cell Signaling to Matrix Remodeling

Linda Irons*, Marcos Latorre, Jay D. Humphrey

Department of Biomedical Engineering,

Yale University, New Haven, CT, USA

*linda.irons@yale.edu

Short title: Cell-Signaling Driven Growth and Remodeling of Arteries

Abstract

Tissue-level biomechanical properties and function derive from underlying cell signaling, which regulates mass deposition, organization, and removal. Here, we couple two existing modeling frameworks to capture associated multiscale interactions and illustrate results for the aorta: one for vessel-level growth and remodeling and one for cell-level signaling. At the vessel level, we employ a constrained mixture model describing turnover of individual wall constituents (elastin, intramural cells, and collagen), which has proven useful in predicting diverse adaptations as well as disease progression using phenomenological constitutive relations. Nevertheless, we now seek an improved mechanistic understanding of these processes, and replace the phenomenological relations in the mixture model with a logic-based signaling model, which yields a system of ordinary differential equations predicting changes in collagen synthesis, matrix metalloproteinases, and cell proliferation in response to altered intramural stress, wall shear stress, and exogenous angiotensin II. This coupled approach promises improved understanding of the role of cell signaling in achieving tissue homeostasis and, importantly, allows us to model feedback between vessel-level mechanics and cell signaling. We verify our model predictions against data from the hypertensive murine infrarenal abdominal aorta and results from validated phenomenological models, and consider effects of noisy signaling parameters and heterogeneous cell populations.

Keywords: mechanobiology, growth and remodeling, constrained mixtures, logic-based modeling, homeostasis

1 Introduction

Soft biological tissues exhibit a remarkable ability to adapt, remodel, and repair in response to diverse stimuli, both normal and injurious. In most cases, these stimuli are sensed by cell surface receptors and associated signals are transduced chemically or mechanically, leading to altered gene expression and gene products. Importantly, many such transcriptional changes alter extracellular matrix composition and organization, orchestrating changes in geometry and biomechanical properties that define much of the tissue functionality. Over the past decade, we have learned much as a community about cell signaling pathways and computational frameworks for analysis are now available.[24] We have similarly learned much about mechanoregulation of extracellular matrix at the tissue level and computational frameworks enable associated growth and remodeling (G&R) to be described and predicted.[1] A continuing challenge, however, has been coupling of cell signaling and tissue-level G&R models to enable modeling from transcript to tissue. Coupled models of this type, which capture feedback between cell signaling and tissue mechanics, promise to provide improved mechanistic insight into tissue remodeling by allowing detailed studies of the role of specific signaling proteins and pathways. In addition, they uniquely allow for the study of disrupted signaling or targeted interventions and resulting effects on potential tissue maladaptations.

Here, we present a new multiscale coupling of a logic-based cell signaling model[15] and a constrained mixture-based model of soft tissue G&R[13,18,27], motivated by the fundamental need to capture changes in cell phenotype and associated changes in deposition and degradation of individual components of the extracellular matrix. We view a mixture-level balance of mass equation as central to coupling outputs of the cell signaling model to inputs in the constrained mixture model, which enables negative feedback as befits tissue homeostasis or, alternatively, positive feedback as

a driver of many disease processes.[14] For illustrative purposes, we focus on homeostatic control of arterial G&R in response to sustained changes in blood pressure and flow. Consistent with the majority of both the available data (*e.g.*, PCR, Western blots, and bulk RNAseq) and prior stress analyses (in terms of mean values of the primary components of stress), we consider a radially homogenized wall with cell signaling focusing on two primary intramural cells of the arterial wall, smooth muscle cells and fibroblasts, with effects of endothelial cells restricted to flow-induced changes in nitric oxide (NO) and endothelin-1 (ET1), which affect matrix synthesis as well as vaso-regulation of the lumen.

2 Materials and Methods

The proposed coupled model is outlined in Fig 1. Under imposed changes in blood pressure and flow, we calculate tissue-level changes in intramural and wall shear stress, which depend on material properties, wall geometry, and fold-changes in applied loads. These stresses form inputs to the cell signaling model, outputs of which govern phenotypic modulation of cells and associated turnover of extracellular matrix. The resulting tissue turnover affects the stresses, which feedback to the cell signaling model, and so forth. In this way, we can model homeostatic processes and, importantly, determine when they are compromised or lost. Of note are the widely separated timescales between G&R (days, weeks, months) and signaling processes (seconds, minutes, hours). Relatively, the stress inputs to the signaling network change slowly, thus it is reasonable, and computationally efficient, to assume both quasi-static mechanics and steady state cell signaling within G&R timesteps (1 day). Thus, ordinary differential equations (ODEs) for cell signaling reduce to nonlinear algebraic equations.

The arterial wall consists of three primary layers (intima, media, and adventitia) and three primary cell types (endothelial cells—EC, smooth muscle cells—SMC, and fibroblasts—FB). The inner layer (intima) and associated ECs are critical for hemostasis and mechanobiological control of the wall, but are negligible mechanically. The media and adventitia can be modeled separately,[4] though radially ho-

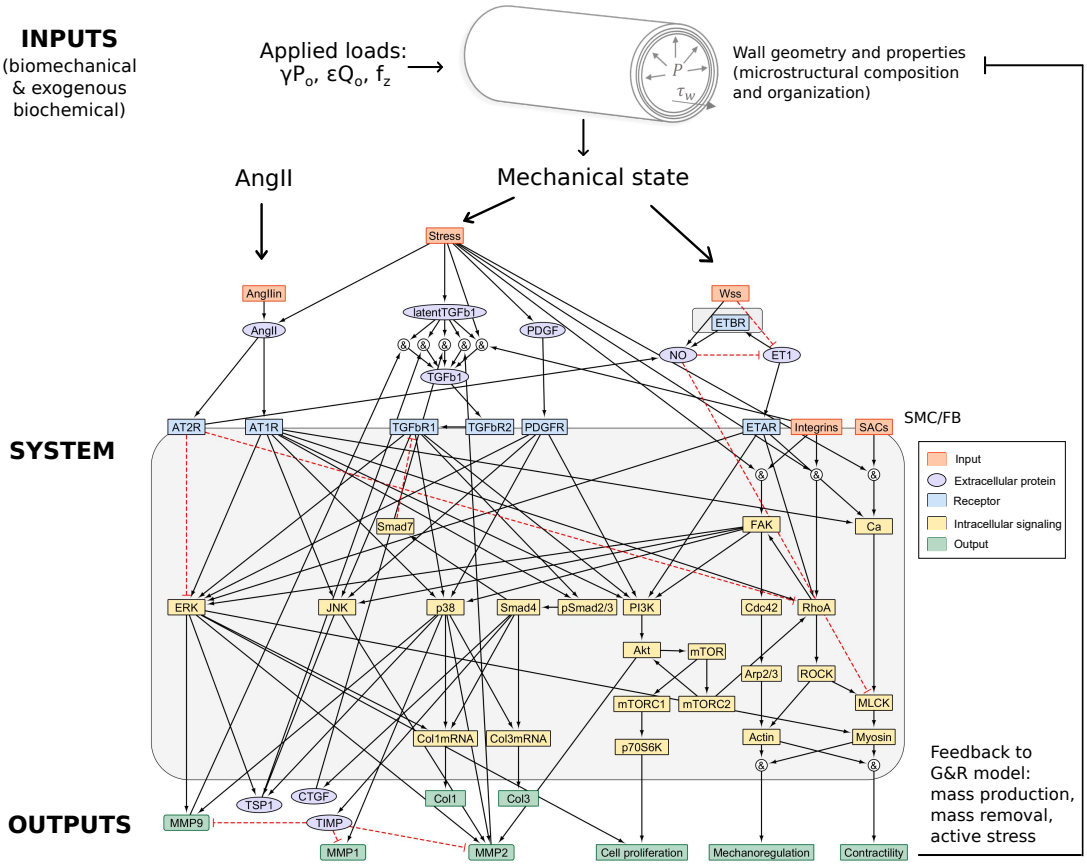

Figure 1: Multiscale coupling between vessel-level growth and remodeling (G&R) processes and cell signaling. Under imposed changes in pressure, flow, and axial load (γP_o, εQ_o, f_z, where γ and ε denote fold-changes from original homeostatic values, subscript o), a constrained mixture G&R model calculates changes in intramural and wall shear stress, which depend on the wall geometry, properties, and applied loads. These changes in mechanical state feed into a logic-based network model, containing 52 species and 89 reactions (see Supplementary Material), to determine corresponding changes in cell signaling. Black solid lines denote activation, red dotted lines inhibition, and the '&' symbol denotes the logical 'AND' operation. For clarity, inhibition is shown to affect a node directly; however, an 'AND NOT' logic operation is used with all incoming reactions to the node. Outputs from the network model directly affect matrix turnover and contractility, which can be incorporated into the G&R framework, providing (generally negative) feedback via the resulting changes in stresses at the vessel level. Network visualization was carried out using Cytoscape (Shannon, 2003) and Netflux (https://github.com/saucermanlab/Netflux).

mogenized models using mean wall stress prove useful given the residual stress field that reduces the gradients in stress.[8,7] Similarly, cells can be studied separately (*e.g.*, immunofluoresence and single cell RNAseq), yet most data come from homogenates of the wall (PCR, Western blots, bulk RNAseq). Therefore, we propose a first generation model based on homogenized wall mechanics and intramural cell (SMC, FB) behaviors.

Cell signaling model

We use our previously described logic-based network for homogenized arterial wall cell signaling,[15] but introduce minor updates to the network structure. The additional species and reactions, with supporting literature, are listed in the Supplementary Material. We consider activation and inhibition across 52 species of interest, with 89 reactions described by logic operators 'AND', 'OR', and 'NOT', modeling conditional dependencies between species. We focus on six main pathways (Smad, p38, ERK, JNK, PI3K/mTOR, RhoA/ROCK) that regulate matrix turnover (collagen synthesis, production of matrix-degrading enzymes MMP-1, -2, and -9), cell proliferation, and contractility, with relations inferred from the literature.[15]

Briefly, each species has a normalized value between 0 and 1, given at time t by

$$\boldsymbol{y}(t) = [y_1(t), \ldots, y_{52}(t)]. \tag{1}$$

General evolution of $\boldsymbol{y}(t)$ is governed by a system of ODEs, built from logic statements describing species interactions (listed in Supplementary Material). In contrast to Boolean logic, this formulation herein (see Kraeutler *et al.*[16]) allows continuous species values in the range $[0, 1]$. Activation by a single variable, $X \in [0, 1]$, is modeled by a normalized Hill function of the form

$$F(X) = \frac{BX^n}{K^n + X^n}, \tag{2}$$

where n is the Hill coefficient, controlling the steepness of the sigmoid. Additionally, $F(0) = 0$ and constants B and K enforce

$$F(1) = 1 \quad \text{and} \quad F(EC_{50}) = 0.5, \tag{3}$$

where EC_{50} is the value of X at which a half-maximal activation occurs, namely,

$$B = \frac{{EC_{50}}^n - 1}{2{EC_{50}}^n - 1} \quad \text{and} \quad K = (B-1)^{1/n}, \tag{4}$$

where, for B to remain positive, ${EC_{50}}^n < 1/2$. Conditional 'AND' ($\wedge$), 'OR' ($\vee$) and 'NOT'($\neg$) operators allow multivariable activation or inhibition (modeled by negation, $1 - F(X)$), through

$$\text{(a)} \;\; X \wedge Y = F(X)F(Y), \tag{5}$$

$$\text{(b)} \;\; X \vee Y = F(X) + F(Y) - F(X)F(Y), \tag{6}$$

$$\text{(c)} \;\; X \wedge \neg Y = F(X)\left(1 - F(Y)\right). \tag{7}$$

These operators are used recursively for more than two species, with ODEs built in a modular fashion using Eq 2 for activation, its negation for inhibition, and the operations in Eqs 5–7. Each reaction is also scaled by a weight parameter, w, and each node has a decay timescale τ[16,15], although this parameter does not feature in the steady state equations. Additionally, each node has a maximal activity level, $Y_{max} \in [0, 1]$; by default $Y_{max} = 1$, although node knockdowns can be simulated by reducing this. An illustrative example showing model construction and governing equations is provided in our previous work.[15]

For specified primary inputs (y_1–y_5: intramural stress, wall shear stress, exogenous AngII, stretch-activated channels (SACs), and integrins), which could be constant or time-dependent, evolving the ODEs provides timecourses for each species. Alternatively, for constant inputs, we can numerically calculate the network steady state from a coupled system of nonlinear equations (see Appendix S4 in previous work[15]).

Previously, we optimized basal input levels and network parameters to best match qualitative input–output data from the arterial literature.[15] By evolving the system to steady state using optimal inputs and parameters, we obtain the basal (presumed homeostatic, in health) state of each species in the network,

$$\boldsymbol{y}_o = [y_{1o}, \ldots, y_{52o}], \tag{8}$$

where the subscript o denotes the original homeostatic state. A homeostatic network

state will be used as the initial state, $\boldsymbol{y}(0) = \boldsymbol{y}_o$, at time $s = 0$ in the G&R model, although new optimal parameters will be found, accounting for quantitative data.

G&R model

We use a constrained mixture model[13] to model the evolving wall mechanics and consider three primary load-bearing constituents: elastin-dominated, collagen-dominated (with four families of fibers), and smooth muscle cell-dominated. These constituents have mass densities ρ_R^e, ρ_R^c, and ρ_R^m, respectively, where the subscript R denotes referential quantities defined with respect to the unit reference volume, with current mass fractions ϕ^e, ϕ^c, and ϕ^m satisfying $\sum_\alpha \phi^\alpha = 1$, where $\alpha = \{e, c, m\}$. We summarize constitutive relations and equilibrium equations below, noting that this general framework has been described previously.[27,18]

Equilibrium and constitutive relations

We model the vessel as a thin-walled, axisymmetric, single-layered cylinder with quasi-static equilibrium, yielding mean circumferential and axial components of the Cauchy stress

$$\sigma_{\theta\theta} = \frac{Pa}{h}, \tag{9}$$

and

$$\sigma_{zz} = \frac{f_z}{\pi h(2a + h)}, \tag{10}$$

where P is the luminal pressure, a inner radius, h wall thickness, and f_z axial force. Constitutively, the Cauchy stress tensor is

$$\boldsymbol{\sigma} = \sum_\alpha \boldsymbol{\sigma}^\alpha - p\boldsymbol{I}, \tag{11}$$

where p is a Lagrange multiplier enforcing incompressibility during transient loading at a fixed G&R time, with $\boldsymbol{\sigma}^\alpha$ mixture-level Cauchy stresses at G&R time s

$$\boldsymbol{\sigma}^\alpha(s) = \frac{1}{\rho}\int_{-\infty}^{s} m^\alpha(\tau) q^\alpha(s,\tau) \hat{\boldsymbol{\sigma}}^\alpha(s,\tau) d\tau, \tag{12}$$

for the $\alpha = \{e, c, m\}$ constituents, where ρ is the total mass density of the vessel (assumed constant), $m^\alpha(\tau) > 0$ the constituent-specific mass production rate, $q^\alpha(s,\tau) \in [0,1]$ the 'survival function' for material deposited at time $\tau \leq s$ that

remains at time s, and $\hat{\boldsymbol{\sigma}}^{\alpha}(s,\tau)$ the constituent-level Cauchy stress,

$$\hat{\boldsymbol{\sigma}}^{\alpha}(s,\tau) = \frac{2}{\det \boldsymbol{F}^{\alpha}_{n(\tau)}(s)} \boldsymbol{F}^{\alpha}_{n(\tau)}(s) \frac{\partial \hat{W}^{\alpha}(\boldsymbol{C}^{\alpha}_{n(\tau)}(s))}{\partial \boldsymbol{C}^{\alpha}_{n(\tau)}(s)} \boldsymbol{F}^{\alpha^T}_{n(\tau)}(s). \tag{13}$$

Here, $\boldsymbol{F}^{\alpha}_{n(\tau)}(s) = \boldsymbol{F}(s)\boldsymbol{F}^{-1}(\tau)\boldsymbol{G}^{\alpha}(\tau)$ are deformation gradients with respect to evolving natural configurations, $n(\tau)$,[13] in which $\boldsymbol{F}(\tau)$ is the mixture deformation gradient and $\boldsymbol{G}^{\alpha}(\tau) = \mathrm{diag}\,[G^{\alpha}_r, G^{\alpha}_{\theta}, G^{\alpha}_z]$ are deposition stretch tensors for each constituent, with $\det \boldsymbol{G}^{\alpha}(\tau) = 1$. Constituent-specific right Cauchy-Green tensors are $\boldsymbol{C}^{\alpha}_{n(\tau)}(s) = \boldsymbol{F}^{\alpha^T}_{n(\tau)}(s)\boldsymbol{F}^{\alpha}_{n(\tau)}(s)$, and $\hat{W}^{\alpha}(\boldsymbol{C}^{\alpha}_{n(\tau)}(s))$ denote constituent-level stored energy density functions. The mixture-level deformation gradient $\boldsymbol{F}(s) = \mathrm{diag}\,[\lambda_r, \lambda_{\theta}, \lambda_z]$, where mixture-level principal stretches

$$\lambda_r = \frac{h(s)}{h(0)} \quad \text{and} \quad \lambda_{\theta} = \frac{a(s) + h(s)/2}{a(0) + h(0)/2}, \tag{14}$$

are derived geometrically and λ_z is prescribed (here, $\lambda_z = 1$ since the *in vivo* configuration is taken as the reference configuration, where deposition stretches are non-unity). The Jacobian determinant $J = \det \boldsymbol{F}$, corresponding to volumetric changes, is $J(s) = \lambda_r \lambda_{\theta} \lambda_z$.

Elastin-dominated matrix is described by a neo-Hookean stored energy density function

$$\hat{W}^{e}(\boldsymbol{C}^{e}_{n(0)}(s)) = \frac{c^e}{2}\left(\mathrm{tr}\left(\boldsymbol{C}^{e}_{n(0)}(s)\right) - 3\right), \tag{15}$$

where $\boldsymbol{C}^{e}_{n(0)}(s) = \mathrm{diag}\left[\lambda_r^2 G_r^{e^2}, \lambda_{\theta}^2 G_{\theta}^{e^2}, \lambda_z^2 G_z^{e^2}\right]$.

Passive mechanics of the smooth muscle cells are given by a Fung-type stored energy density function,

$$\hat{W}^{m}(\lambda^{m}_{n(\tau)}(s)) = \frac{c_1^m}{4c_2^m}\left(\exp\left(c_2^m\left(\lambda^{m}_{n(\tau)}(s)^2 - 1\right)^2\right) - 1\right), \tag{16}$$

where stretches $\lambda^{m}_{n(\tau)}(s)$ depend on both mixture-level principal stretches (at times s and τ) and constituent-level deposition stretches (at deposition time τ).

For collagen, we consider four predominant families of fibers[18,4], with fractions β_{θ}, β_z, β_{d^+}, and β_{d^-} for circumferential, axial, and symmetric diagonal fibers, respectively, with diagonal fibers oriented at an angle of $\pm\alpha_0$ from the axial direction.

The contribution of each fiber family is

$$\hat{W}^{c_i}\left(\lambda^{c_i}_{n(\tau)}(s)\right) = \frac{c^c_1}{4c^c_2}\left(\exp\left(c^c_2\left(\lambda^{c_i}_{n(\tau)}(s)^2 - 1\right)^2\right) - 1\right), \tag{17}$$

which depend on orientation-specific stretches, $\lambda^{c_i}_{n(\tau)}(s)$, for each family, with $i = \{\theta, z, d^+, d^-\}$.

Similarly to Eq 12, production and removal of a constituent α determines its homogenized mass density per unit reference volume through

$$\rho^\alpha_R(s) = \int_{-\infty}^{s} m^\alpha_R(\tau) q^\alpha(s,\tau) d\tau, \tag{18}$$

where $m^\alpha_R = J m^\alpha$ is the referential mass density production rate, with $J = \sum_\alpha \rho^\alpha_R/\rho = \det\boldsymbol{F}$ relating changes in mass and volume. For more details of the above formulation, see previous works.[13,27,18]

Coupling between G&R and signaling models

We now formulate the multiscale coupling; stresses from the G&R model (Eq 11) are scaled to form appropriate inputs for the network model, and network outputs influence vessel-level G&R through their effect on matrix turnover (via Eq 12).

From G&R to signaling inputs

To initialize computational simulations of constrained mixture models of arterial G&R, one prescribes an initial vessel geometry, material properties, mass fractions and deposition stretches, then uses equilibrium equations to determine the associated initial pressure, axial load, and homeostatic Cauchy stress, $\boldsymbol{\sigma}_o$. For convenience, we use the first invariant of the Cauchy stress as a scalar-valued measure of intramural stress

$$\tilde{\sigma} = \mathrm{tr}\boldsymbol{\sigma}, \tag{19}$$

and consider normalized changes in stress from the initial homeostatic state as

$$\Delta\sigma = \frac{\tilde{\sigma} - \tilde{\sigma}_o}{\tilde{\sigma}_o}. \tag{20}$$

Similarly, for wall shear stress, normalized changes are

$$\Delta\tau_w = \frac{\tau_w - \tau_{w_o}}{\tau_{w_o}} = \frac{\epsilon a_o^3}{a^3} - 1, \tag{21}$$

assuming fully-developed laminar flow ($\tau_w = 4\mu Q/\pi a^3$, where Q is the flow rate, μ viscosity, a the inner radius) and a fold-change in flow rate, $\varepsilon = Q/Q_o$.

Let the homeostatic wall stress, $\tilde{\sigma}_o$, map onto the basal stress input of the network model $y_{Stress}(0)$, via linear scaling

$$y_{Stress}(s) = \frac{\tilde{\sigma}}{\tilde{\sigma}_o} y_{Stress}(0), \tag{22}$$

where the current network stress input $y_{Stress}(s)$ recovers the original value when $\tilde{\sigma}$ equals its homeostatic value. Similarly, let the scaled wall shear stress input to the network model be

$$y_{Wss}(s) = \frac{\tau_w}{\tau_{w_o}} y_{Wss}(0) = \varepsilon \frac{a_o^3}{a^3} y_{Wss}(0). \tag{23}$$

We will find optimal values of $y_{Stress}(0)$ and $y_{Wss}(0)$ during model parameterization.

From signaling outputs to G&R

At each G&R timestep we calculate the resulting output of all 52 species in response to the scaled inputs (Eqs 22, 23). Although the state of every species is available and important, we focus on outputs especially relevant to matrix turnover and thus tissue-level biomechanical properties. Collagen is degraded by numerous matrix metalloproteinases, including MMP1, MMP2, and MMP9, which respectively cut the collagen molecule and degrade its fragments.[28] We take their mean value to obtain a normalized "proteolytic burden" between 0 and 1, namely

$$\psi_m(s) = \frac{y_{MMP1}(s) + y_{MMP2}(s) + y_{MMP9}(s)}{3}. \tag{24}$$

This is equivalent to using their sum (via a scale factor that would arise later), and we renormalize to $[0, 1]$ at this stage for convenience. For collagen production, we similarly consider together collagen I and III, the two primary fibrillar types, noting that other matrix constituents contribute to collagen fibrillogenesis that are not modeled explicitly. Since we do not distinguish subtypes in the G&R model, we combine their effects and take the mean value

$$\psi_c(s) = \frac{y_{Col1}(s) + y_{Col3}(s)}{2}, \tag{25}$$

again renormalizing to $[0, 1]$. Weighted sums could also be considered to account for differing effects of MMP or collagen subtype.

We include intramural cell proliferation as a species, and directly define

$$\psi_p(s) = y_{CellProliferation}(s). \tag{26}$$

At G&R time $s = 0$, the network is at an initial homeostatic state. Denote

$$\psi_{m_o} = \psi_m(0), \quad \psi_{c_o} = \psi_c(0), \quad \text{and} \quad \psi_{p_o} = \psi_p(0). \tag{27}$$

Although we also consider contractile proteins in the network model, we first focus on coupling mass production and degradation.

Mass production and removal functions

Over the timescale of interest, we assume elastin does not turnover whereas rates of collagen and intramural cell turnover depend on the chemo-mechanical state, and thus cell signaling. In this coupled formulation, these rates are informed directly by the network model rather than phenomenologically as in previous tissue-level models; these prior models will serve as important baseline comparators, however, enabling verification and validation of the current coupled framework.

Collagen

Consider a collagen mass density production function of the form

$$m_R^c(s) = \rho_R^m(s)\mathcal{K}_{max}^c\psi_c(s), \tag{28}$$

which is proportional to the mass density of SMCs, $\rho_R^m(s)$, since collagen is produced by intramural cells, dominated by SMCs of the media and FBs of the adventitia. The constant $\mathcal{K}_{max}^c$ is the maximum rate constant for this production (with units 1/time), to be scaled by the dimensionless network output $\psi_c(s) \in [0, 1]$ (Eq 25). Equivalently,

$$m_R^c(s) = \rho_R^m(s)\mathcal{K}_o^c\left(1 + \Delta\psi_c(s)\right), \tag{29}$$

where a basal rate parameter, $\mathcal{K}_o^c$, is

$$\mathcal{K}_o^c = \mathcal{K}_{max}^c\psi_{c_o}, \tag{30}$$

and

$$\Delta\psi_c = \frac{\psi_c(s) - \psi_{c_o}}{\psi_{c_o}}. \tag{31}$$

To find the basal rate parameter, $\mathcal{K}_o^c$, consider G&R time $s = 0$. Assuming homeostasis at all earlier times, with $\rho_R^\alpha(s < 0) = \rho_o^\alpha$, the integral in Eq 18 constrains mass production and removal to balance. Following previous formulations[27,18], let a first-order kinetics type survival function for material deposited at time $\tau \leq s$ that survives at time s be

$$q^c(s,\tau) = \exp\left(-\int_\tau^s k^c(t)\mathrm{d}t\right), \tag{32}$$

where the removal rate, $k^c(t)$, is the constant k_o^c at homeostatic times $s < 0$. Eq 18 then yields

$$\rho_o^m \mathcal{K}_o^c = \rho_o^c k_o^c, \tag{33}$$

where k_o^c denotes the homeostatic removal rate (determined from the half-life of collagen), with initial mass densities (calculated from histological mass fractions) assumed known. Thus,

$$\mathcal{K}_o^c = \frac{\rho_o^c}{\rho_o^m} k_o^c, \tag{34}$$

and, substituting this into Eq. 29, collagen mass production is

$$m_R^c(s) = \frac{\rho_R^m(s)\rho_o^c k_o^c}{\rho_o^m}\left(1 + \Delta\psi_c(s)\right), \tag{35}$$

where $\rho_o^c k_o^c$ is the total basal removal rate and $\rho_R^m(s)/\rho_o^m$ accounts for changes in intramural cell mass density by scaling the basal network response to a tissue-level mass production; if intramural cells increase (whilst each maintaining a fixed production), so too would their total collagen synthesis.

Note that collagen mass production is stimulated by $\Delta\psi_c(s)$ which depends, via the network model, on changes in the intramural and wall shear stresses, whereas previous phenomenological stimuli depend linearly on changes in stress via 'gain' parameters. Following previous approaches, we define a phenomenological mass production function[27,18], to later compare to the network approach. Let

$$\hat{m}_R^c(s) = \frac{\rho_R^m(s)\rho_o^c k_o^c}{\rho_o^m}\left(1 + K_\sigma^c\Delta\sigma - K_\tau^c\Delta\tau_w\right), \tag{36}$$

where K_σ^c and K_τ^c are dimensionless gain parameters associated with normalized changes in intramural stress ($\Delta\sigma$, Eq 20) and wall shear stress ($\Delta\tau_w$, Eq. 21), respectively, from homeostatic.

We define the removal rate, $k^c(s)$, used in Eq 32, by

$$k^c(s) = \zeta(s) k^c_{max} \psi_m(s), \tag{37}$$

with k^c_{max} a maximal removal rate that scales the proteolytic burden $\psi_m(s) \in [0, 1]$. Similarly to the scale factor $\rho^m_R(s)/\rho^m_o$ in Eq. 35, $\zeta(s)$ scales cell-level proteolytic network outputs to a tissue-level removal rate, via

$$\zeta(s) = \frac{\rho^m_R(s)}{\rho^m_o} \frac{\rho^c_o}{\rho^c_R(s)}, \tag{38}$$

where $\zeta(0) = 1$. For relative increases in the mass density of intramural cells (each producing MMPs at a fixed rate) to collagen, there will overall be more collagen removal. For increases in collagen relative to intramural cells, with cells degrading collagen at a fixed rate, the collagen removal rate at the population level will be reduced. Equivalently,

$$k^c(s) = \zeta(s) k^c_o \left(1 + \Delta\psi_m(s)\right), \tag{39}$$

where

$$k^c_o = k^c_{max} \psi_{m_o}, \tag{40}$$

is the homeostatic removal rate, and

$$\Delta\psi_m(s) = \frac{\psi_m(s) - \psi_{m_o}}{\psi_{m_o}}. \tag{41}$$

Again we introduce a phenomenological removal rate[18] for comparison, driven directly by changes in intramural stress via

$$\hat{k}^c(s) = \zeta(s) k^c_o \left(1 + (\Delta\sigma)^2\right). \tag{42}$$

Intramural cells

In general, intramural cell and collagen stimuli differ (although they have been assumed equal or proportional in previous work). We include cell proliferation explicitly in our network model (Fig 1), and thus let mass production be

$$m^m_R(s) = \rho^m_R(s) \mathcal{K}^m_{max} \psi_p(s), \tag{43}$$

proportional to $\rho_R^m(s)$, the mass density of cells that can proliferate, with $\mathcal{K}_{max}^m$ a maximal proliferation rate to scale the network output $\psi_p \in [0,1]$.

Stress-driven cell apoptosis or anoikis can be crucial, but we do not currently account for it in the network. Rather, consider a general first order decay of intramural cells (to capture baseline apoptosis), via the survival function for cells deposited at time $\tau \leq s$ and surviving at time s, namely

$$q^m(s,\tau) = \exp\left(-\int_\tau^s k^m(t)\mathrm{d}t\right), \tag{44}$$

with constant basal decay rate

$$k^m(s) = k_o^m. \tag{45}$$

The balance of production and removal at $s = 0$ requires

$$\rho_o^m \mathcal{K}_{max}^m \psi_{p_o} = \rho_o^m k_o^m, \tag{46}$$

or

$$\mathcal{K}_{max}^m = k_o^m / \psi_{p_o}. \tag{47}$$

Intramural cell mass production is therefore

$$m_R^m(s) = \rho_R^m(s) k_o^m (1 + \Delta\psi_p(s)), \tag{48}$$

where

$$\Delta\psi_p(s) = \frac{\psi_p(s) - \psi_{p_o}}{\psi_{p_o}}. \tag{49}$$

We will again compare the network-driven results to those generated using phenomenological mass production and removal functions[27,18], given by

$$\hat{m}_R^m(s) = \rho_R^m(s) k_o^m \left(1 + K_\sigma^m \Delta\sigma - K_\tau^m \Delta\tau_w\right), \tag{50}$$

where K_σ^m and K_τ^m are dimensionless gain parameters associated with normalized changes in intramural and wall shear stresses from homeostatic, and[18]

$$\hat{k}^m(s) = k_o^m \left(1 + (\Delta\sigma)^2\right). \tag{51}$$

In summary, G&R-determined intramural and wall shear stresses enter the network model via Eqs 22 and 23. Cell-signaling driven mass production and removal provide feedback to the G&R model via Eqs 35, 39, 45, and 48.

3 Results

3.1 Experimental validation

First, consider a published experimental dataset[6] that quantifies hypertensive remodeling of the infrarenal abdominal aorta in apolipoprotein-E null ($ApoE^{-/-}$) mice in response to 28 days of AngII infusion. These data have also been modeled using a bilayered constrained mixture model with phenomenological mass production and removal rates[21], thus we use material parameters obtained therein (via nonlinear regression of experimental pressure-diameter and axial force-length curves), homogenized here for our single-layered model (Table 1).

We further parameterized our coupled model to capture the observed G&R via evolved values of ρ^c_R/ρ^c_o and ρ^m_R/ρ^m_o calculated from histological data at day 28.[6] Free parameters in the coupled model are initial network inputs: $y_{Stress}(0)$, $y_{Wss}(0)$, $y_{AngIIin}(0)$, and $y_{Integrins}(0)$, and three Hill parameters, w, n, and EC_{50}. To simplify parameterization given the absence of detailed cell signaling data, we assume uniform Hill parameters across the network (*i.e.* the same w, n, and EC_{50} for each reaction), consistent with previous studies that yielded successful model predictions.[15,16,24,26] Whilst eventually desirable, varying these parameters for each reaction will require considerable cell-level data to ensure unique parameterization. Finally, we must specify the fifth input, $y_{SACs}(0)$, although this value does not influence outputs of interest and requires contractility measurements to be uniquely determined. We obtained best-fit values for the seven free parameters (with $y_{SACs}(0) = 0.25$ prescribed) via least squares nonlinear regression, only minimizing the error in evolved referential mass densities at day $s = 28$. The parameters are bounded; model inputs and weights must lie between 0 and 1, and Hill parameters were constrained within conservative ranges $0.4 < EC_{50} < 0.8$ and $1 < n < 3$ (whilst also obeying ${EC_{50}}^n < 1/2$), which are reasonable based on prior analyses.

The experimental data and coupled model predictions are shown in Fig 2. Whereas evolved referential mass densities were used in the fit, good predictions emerged for the evolving geometry (inner radius, a/a_o, and wall thickness, h/h_o) and circumfer-

Artery mass density	ρ	1050 kg/m^3
Initial mass fractions	ϕ_o^e, ϕ_o^m, ϕ_o^c,	0.079, 0.326, 0.595
Collagen fiber fractions	β_θ, β_z, β_{d+}, β_{d-}	0.058, 0.057, 0.4425, 0.4425
Diagonal fiber orientation	α_0	30.7°
Initial inner radius, thickness	a_o, h_o	0.417 mm, 0.032 mm
Elastin parameter	c^e	114 kPa
Intramural cell properties	c_1^m, c_2^m	343 kPa, 1.23
Collagen properties	c_1^c, c_2^c	450 kPa, 3.51
Elastin deposition stretches	G_r^e, G_θ^e, G_z^e	$1/(G_\theta^e G_z^e)$, 1.96, 1.73
Cell deposition stretches	G_θ^m	1.17
Collagen deposition stretches	$G_\theta^c = G_z^c = G_{d+}^c = G_{d-}^c$	1.20
Mass removal rates	k_o^m, k_o^c	1/10 day^{-1}, 1/10 day^{-1}

Table 1: Parameters for the murine infrarenal abdominal aorta, homogenized for a single-layered G&R model based in part on a previous bilayered parameter fitting to experimental data.[21]

ential and axial stresses ($\sigma_{\theta\theta}$, σ_{zz}). Notably, predictions at early times (days 0, 4, 7, 14) were better than previous phenomenological model fits.[21] Nevertheless, inner radius was underestimated at days 21 and 28, as before[21], where additional terms for inflammation (not considered here) were required to improve the fit.

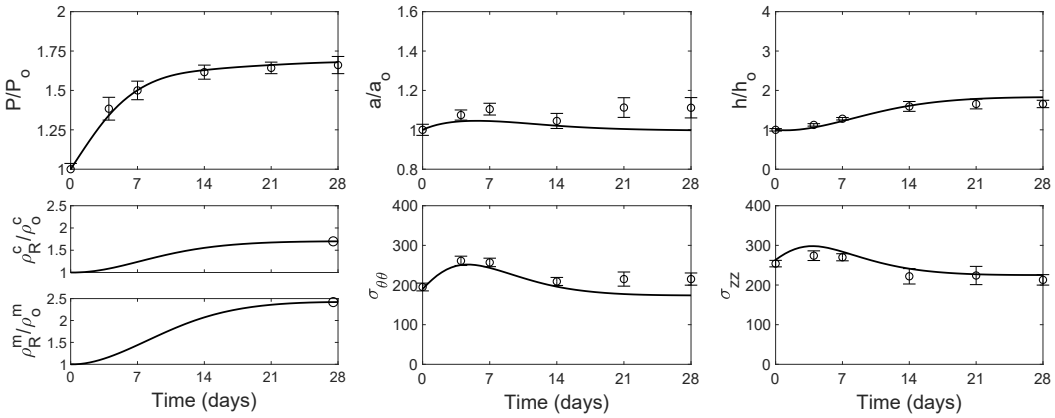

Figure 2: Experimental data (circle ± error bars)[6] and coupled model predictions (solid lines) of the evolving infrarenal abdominal aorta geometry (inner radius, a/a_o, and wall thickness, h/h_o) and circumferential and axial stresses ($\sigma_{\theta\theta}$, σ_{zz}) in response to a 68% increase in pressure over 28 days. Material parameters are given in Table 1 and network model parameters were fit to the referential mass densities of collagen and intramural cells (ρ_R^c/ρ_o^c, ρ_R^m/ρ_o^m) at day 28 (open circles), resulting in best-fit values: $y_{Stress}(0) = 0.163$, $y_{Wss}(0) = 0.582$, $y_{AngIIin}(0) = 0.113$, $y_{Integrins}(0) = 0.20$, $w = 0.70$, $n = 1.378$, and $EC_{50} = 0.604$ (with $y_{SACs}(0) = 0.25$).

3.2 Correspondence between phenomenological and coupled models

Next, we compare results from our coupled model to a broader range of results generated using previously validated phenomenological mass production and removal functions (Eqs 36, 42, 50, and 51). Such phenomenological functions, which we replace with Eqs 35, 39, 45, and 48 in the coupled model, have long captured diverse experimental datasets; we therefore aim to ensure that our model can produce similar behavior over a broad range of pressure and flow perturbations. We use parameters for a mouse descending thoracic aorta[20] (Table 2), again homogenized for a single-layered G&R model based on prior bilayered parameters.[19]

Artery mass density	ρ	1050 kg/m^3
Initial mass fractions	ϕ_o^e, ϕ_o^m, ϕ_o^c,	0.34, 0.33, 0.33
Collagen fiber fractions	β_θ, β_z, β_{d^+}, β_{d^-}	0.0560, 0.0670, 0.4385, 0.4385
Diagonal fiber orientation	α_0	29.91°
Initial inner radius, thickness	a_o, h_o	0.647 mm, 0.04 mm
Elastin parameter	c^e	89.71 kPa
Intramural cell properties	c_1^m, c_2^m	261.4 kPa, 0.24
Collagen properties	c_1^c, c_2^c	234.9 kPa, 4.08
Elastin deposition stretches	G_r^e, G_θ^e, G_z^e	$1/(G_\theta^e G_z^e)$, 1.9, 1.62
Cell deposition stretches	G_θ^m	1.2
Collagen deposition stretches	$G_\theta^c = G_z^c = G_{d^+}^c = G_{d^-}^c$	1.25
Mass removal rates	k_o^m, k_o^c	1/7 day^{-1}, 1/7 day^{-1}
Intramural cell gain parameters	K_σ^m, K_τ^m	1.6, 2
Collagen gain parameters	K_σ^c, K_τ^c	ηK_σ^m, ηK_τ^m, with $\eta \in [1, 1.25, 1.5]$

Table 2: Baseline parameter set from a previous fit[20] for a mouse descending thoracic aorta, which were homogenized for a single-layered G&R model based on the original bilayered parameter fitting[19]. For the collagen gain parameters, we scale intramural cell gains by η, with values specified in relevant figure captions. The four gain parameters are used in simulating the phenomenological model only.

We generate timecourse G&R data for fifteen pressure and flow combinations, with pressure increasing by 10–50% (in increments of 10%) and flow increasing by 0%, 5%, and 10%, both relative to homeostatic. Using one intermediate combination (a 30% pressure and 5% flow increase), we parameterized the coupled model to capture long-term steady state values of ρ_R^c/ρ_o^c and ρ_R^m/ρ_o^m generated by the phenomenological model. In general, and as in Fig 2, these ratios could be calculated from histological data.[5] We obtained best-fit values of the network inputs and parameters, minimizing the error in steady state mass densities for $100 < s < 200$ days, with parameters bounded by the previously described constraints. Using best-fit parameters, we then simulated the other fourteen combinations of increased pressure and flow (Supplementary Fig S1). For the fitting case (30% pressure and 5% flow increase, highlighted in green in Fig 3), we see strong agreement between the two models; note that geometric variables (inner radius, a, and wall thickness, h) were not used in the fit, but their evolution and end values agree between models. We also show coupled model predictions for four other pressure elevations (ranging from 10% to 50% for a fixed increase in flow of 5%), where the coupled model (solid lines) and phenomenological model (dashed lines) again agreed well (Fig 3), albeit with slight differences in constituent mass densities at the highest pressure ($P/P_o = 1.5$).

Consider, too, the network-informed stimuli for mass production and removal, $\Delta\psi_c$, $\Delta\psi_p$, $\Delta\psi_m$ in Eqs 35, 48, and 39, respectively (Fig 4). All three stimuli increase with pressure, and thus intramural stress, as posited in the phenomenological functions (Eqs 36, 50, and 42, respectively). Additionally, consider three intermediate species, AngII, NO, and ET1. AngII production is stimulated by changes in pressure, and remains elevated after $s = 0$ due to an imposed exogenous AngII source (similar to the experimental protocol from which the original parameters were determined.[5,19]) Interestingly, we see slight reductions in NO and increases in ET1 with pressure. From the network diagram (Fig 1), intramural stress does not directly induce these responses, but the resulting increased inner radius (Fig 3) yields a drop in wall shear stress. This affects NO and ET1, demonstrating how feedback from the tissue-level model influences network dynamics; such responses rely on feedback between

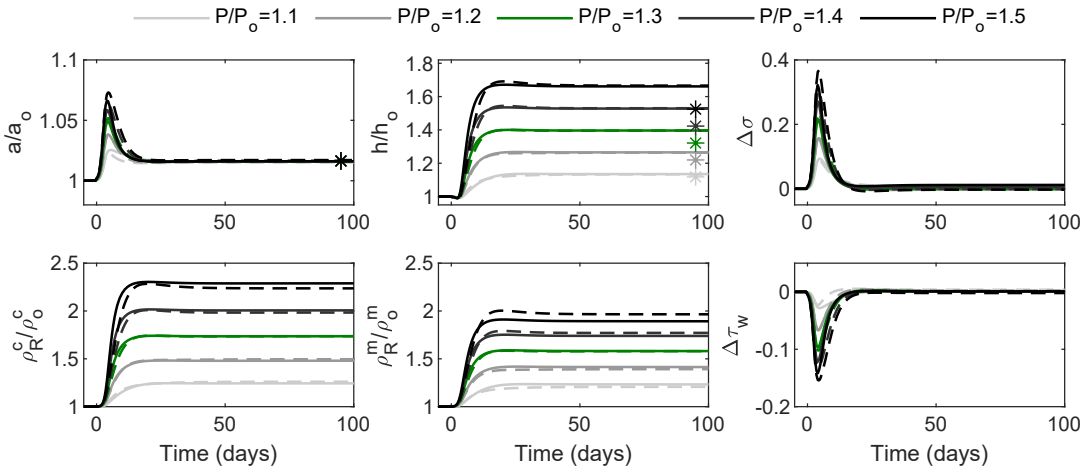

Figure 3: Timecourses for five levels of pressure increase (10–50%) from homeostatic, together with a flow increase of 5%. Solid lines indicate results from the coupled model; dashed lines represent results from the phenomenological model, for parameters in Table 2 with $\eta = 1.25$. The coupled model was fit only to end values of ρ_R^c/ρ_o^c and ρ_R^m/ρ_o^m that were generated by the phenomenological model with $P/P_o = 1.3$ and $Q/Q_o = 1.05$ (highlighted in green) yielding $y_{Stress}(0) = 0.216$, $y_{Wss}(0) = 0.436$, $y_{AngIIin}(0) = 0.20$, $y_{SACs}(0) = 0.248$, $y_{Integrins}(0) = 0.251$, $w = 0.763$, $n = 1.954$, and $EC_{50} = 0.621$. For the inner radius, a, and wall thickness, h, asterisks indicate ideal adaptations, given by $a/a_o \to (Q/Q_o)^{1/3}$ and $h/h_o \to (P/P_o)(Q/Q_o)^{1/3}$, though homeostasis only requires that regulated variables return toward, not precisely to, original values.

mechanics and signaling, and would not have been predicted by the signaling model alone.

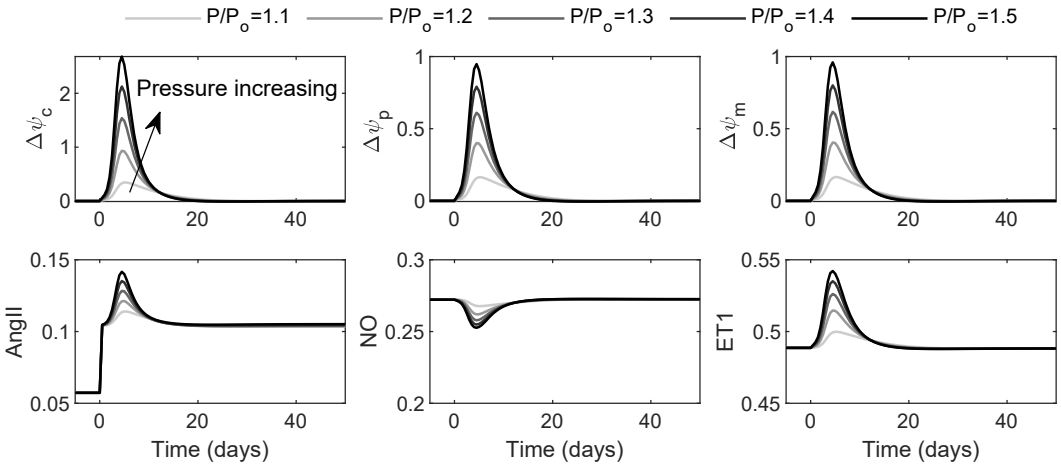

Figure 4: Network-informed stimuli, $\Delta\psi_c$ (collagen), $\Delta\psi_p$ (cell proliferation), $\Delta\psi_m$ (MMPs) (Eqs 35, 48, and 39, respectively) for five levels of pressure increase (10–50%) from homeostatic, together with a flow increase of 5%, and evolution of three network species: AngII, NO and ET1. The coupled model uses $y_{Stress}(0) = 0.216$, $y_{Wss}(0) = 0.436$, $y_{AngIIin}(0) = 0.20$, $y_{SACs}(0) = 0.248$, $y_{Integrins}(0) = 0.251$, $w = 0.763$, $n = 1.954$, and $EC_{50} = 0.621$. Exogenous AngII was applied via a sustained input $y_{AngIIin}(s > 0)$, which is a free parameter in the fitting process. Note the mild transient increase in ET1 (when the wall distends elastically, thus reducing flow-induced shear stress) and complementary decrease in NO, as expected. There are transient (stress-driven) increases in AngII in addition to the sustained increase due to exogenous AngII.

Similarly good results emerge for the predicted effect of varying flow (Supplementary Fig S2) with a fixed pressure increase (30%), again with inner radius adapting ideally ($a \to \epsilon^{1/3} a_o$) but the wall thickening to a value slightly greater than ideal ($h > \gamma\epsilon^{1/3} h_o$). Network-informed stimuli for mass production and removal, $\Delta\psi_c$, $\Delta\psi_p$, $\Delta\psi_m$ decrease with flow (Supplementary Fig S3), and thus with wall shear stress, as posited in the phenomenological rate functions (Eqs 36, 50, and 42, respectively).

To summarise the data from all fifteen pressure-flow combinations (Supplementary Fig S1), we compare here the steady state values of each of six key variables as a function of pressure and flow (Fig 5). Grey surfaces represent predictions from

the coupled model, whereas red meshes show corresponding results from the phenomenological model. Although we only fit to ρ_R^c/ρ_o^c and ρ_R^m/ρ_o^m at one combination in this space ($P/P_o = 1.3$, $Q/Q_o = 1.05$), there is close agreement across the different combinations and variables, including the stress differences that drive the models. The largest deviation appeared for intramural cell mass density, which is underestimated in the coupled model compared to the phenomenological model at high pressures. Here we used $\eta = 1.25$ as the scale factor for collagen gain parameters (see Table 2), but we found similarly good results using $\eta = 1$ and $\eta = 1.5$ (Supplementary Figs S4–S11).

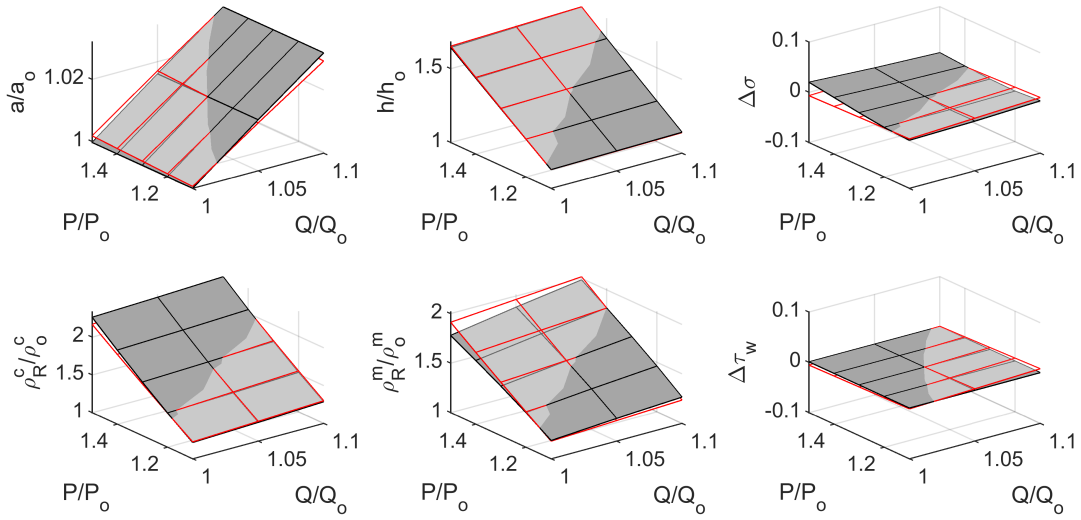

Figure 5: Steady state values for five levels of pressure elevation (10%, 20%, 30%, 40%, 50%) and three levels of flow increase (0%, 5%, 10%) relative to homeostatic for the coupled (grey surface) and phenomenological (red mesh) models, for parameters in Table 2 with $\eta = 1.25$. The coupled model was fit only to end values of ρ_R^c/ρ_o^c and ρ_R^m/ρ_o^m that were generated by the phenomenological model with $P/P_o = 1.3$ and $Q/Q_o = 1.05$, yielding $y_{Stress}(0) = 0.216$, $y_{Wss}(0) = 0.436$, $y_{AngIIin}(0) = 0.20$, $y_{SACs}(0) = 0.248$, $y_{Integrins}(0) = 0.251$, $w = 0.763$, $n = 1.954$, and $EC_{50} = 0.621$.

The coupled model captured the behavior generated by the phenomenological model, which has successfully described experimental data in multiple prior studies. Additionally, this close agreement demonstrates that, for this parameter set, linear phenomenological functions in Eqs 36, 42, 50, and 51 reflect well the more complex underlying signaling, at least under moderate changes in pressure and flow

from homeostatic values. Nevertheless, inclusion of signaling pathways can provide additional mechanistic insight. Particularly, within this framework, we can track and modify intermediate signaling species and exogenous inputs,[15] and introduce stochasticity into the signaling response, which we demonstrate next.

3.3 Sensitivity Analysis

Cell signaling networks are inherently noisy, yet robust in function. Here, we use the coupled framework to investigate the sensitivity of tissue-level outputs to perturbed signaling parameters. We perturb the network in two ways: firstly, with uniformly distributed noise to six of the parameters, $y_{AngIIin}(0)$, $y_{SACs}(0)$, $y_{Integrins}(0)$, w, n, and EC_{50}. The mechanical inputs, $y_{Stress}(0)$ and $y_{Wss}(0)$ remain fixed, but the network ability to sense and transmit these signals vary via the perturbed parameters. For different levels of perturbation (mediated by parameter p), we run 100 simulations with each parameter modified by up to $\pm p\%$ of its best-fit value (Fig 6(a)). For $p = 10$, overlayed timecourses for each simulation (Fig 6(b)) remain close. Transient behaviors and the final constituent mass densities vary slightly, yet the final inner radius and wall thickness are well preserved in each case, exhibiting robustness to small parameter perturbations.

Next, we modify the framework to allow a second type of perturbation: heterogeneous cell populations. We take the same parameters from 100 simulations in Fig 6 and assign them as individual cell parameters as follows. First, we replicate the network and associated ODEs for the $n = 100$ distinct parameter sets. Each network is allocated individual parameters, w_j, n_j, EC_{50_j}, and so forth. The resulting system of equations is large, yet still efficient to solve; although the n networks are coupled through mechanical feedback, their signaling is not directly coupled, thus solution at each G&R timestep is parallelizable. Collective stimuli for collagen and intramural cell mass production and removal are

$$\Delta\psi_i = \frac{1}{n}\sum_{j=1}^{n}\Delta\psi_{ij}, \tag{52}$$

where $i = \{c, p, m\}$ for collagen, intramural cell proliferation, and proteolytic burden, j is the number of distinct parameter sets, and $\Delta\psi_{ij} = (\psi_{ij} - \psi_{ij0})/\psi_{ij0}$ are

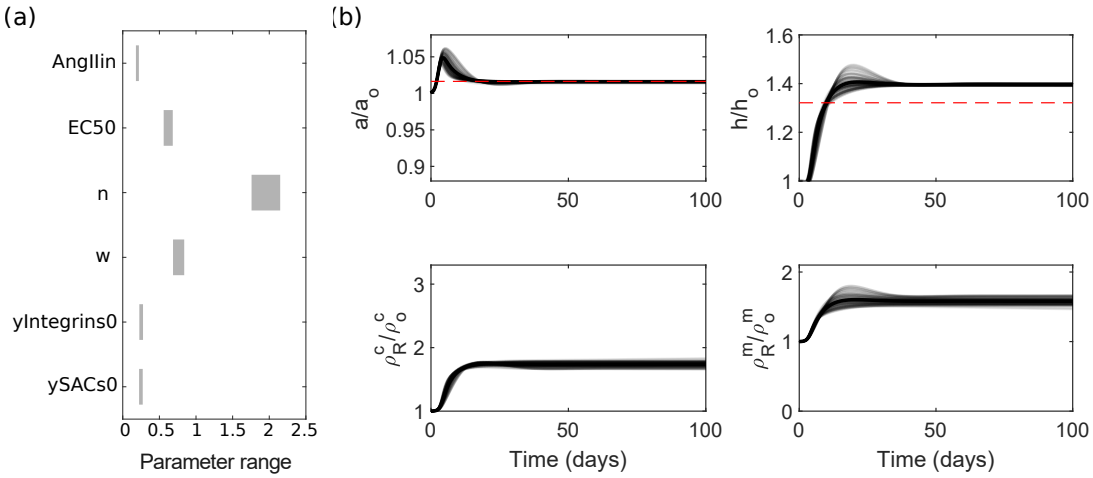

Figure 6: Sensitivity analysis of a single cell signaling network. (a) Parameter ranges, where parameters vary from their best-fit values by uniformly distributed noise of up to ±10% and (b) Overlayed timecourses for 30% pressure and 5% flow increases from homeostatic, where 100 parameter sets were sampled from the ranges shown in (a). Baseline parameters are $y_{Stress}(0) = 0.216$, $y_{Wss}(0) = 0.436$, $y_{AngIIin}(0) = 0.20$, $y_{SACs}(0) = 0.248$, $y_{Integrins}(0) = 0.251$, $w = 0.763$, $n = 1.954$, and $EC_{50} = 0.621$.

calculated as in Eqs 31, 49, and 41, using appropriate network outputs for each cell, ψ_{ij} and ψ_{ij0}, which vary depending on network parameters. Although stimuli can differ significantly for each cell (Fig 7(a)), the collective behavior yields a similar tissue-level result to when there is no noise (Fig 7(b)).

From a biological standpoint, the importance of collective behavior over that of any one cell provides additional protection against individual fluctuations and disrupted signaling. This is further emphasized for larger perturbations of ±20% (Fig 8), where perturbations applied to the network without heterogeneity begin to spread and diverge significantly (Fig 8(b)), whereas these same perturbations applied to individual cells (Fig 8(c,d)) yield tissue-level behavior only slightly differently from baseline.

4 Discussion

Phenomenological models have provided, and continue to provide, considerable insight into the G&R of biological soft tissues.[17,9,3,1] Recently, for example, such a

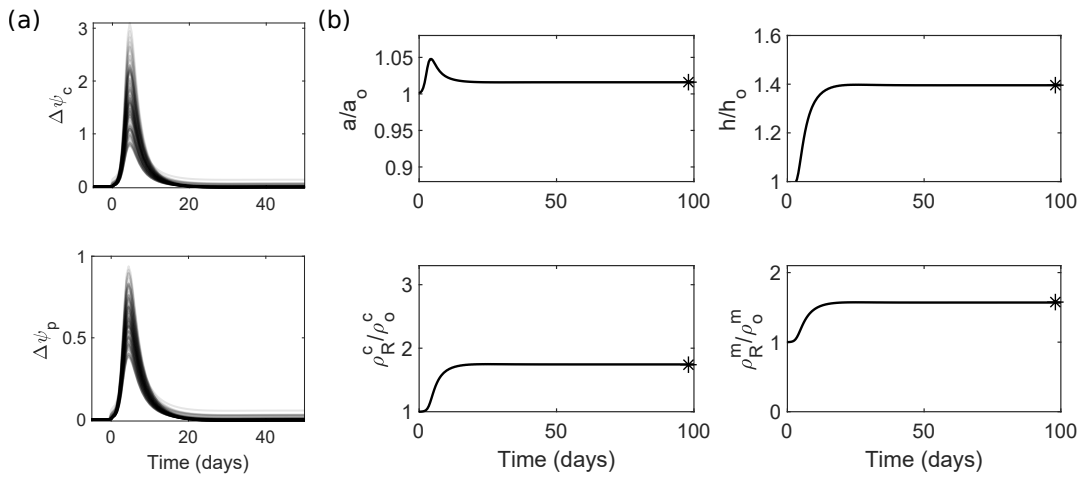

Figure 7: Sensitivity analysis of a heterogeneous population of cells with collective behavior. (a) Overlayed collagen and intramural cell mass production stimuli, given by $\Delta\psi_c$ and $\Delta\psi_p$, respectively (Eqs 35, 48), for 100 cells which each contribute equally to collective stimuli (Eq 52), and (b) Resulting timecourses for 30% pressure and 5% flow increases from homeostatic. The 100 parameter sets for individual cells are the same as those used in Fig 6, which vary by up to ±10% from baseline values: $y_{AngIIin}(0) = 0.20$, $y_{SACs}(0) = 0.248$, $y_{Integrins}(0) = 0.251$, $w = 0.763$, $n = 1.954$, and $EC_{50} = 0.621$. Additionally, $y_{Stress}(0) = 0.216$ and $y_{Wss}(0) = 0.436$. Asterisks indicate the values obtained under baseline conditions (no perturbations).

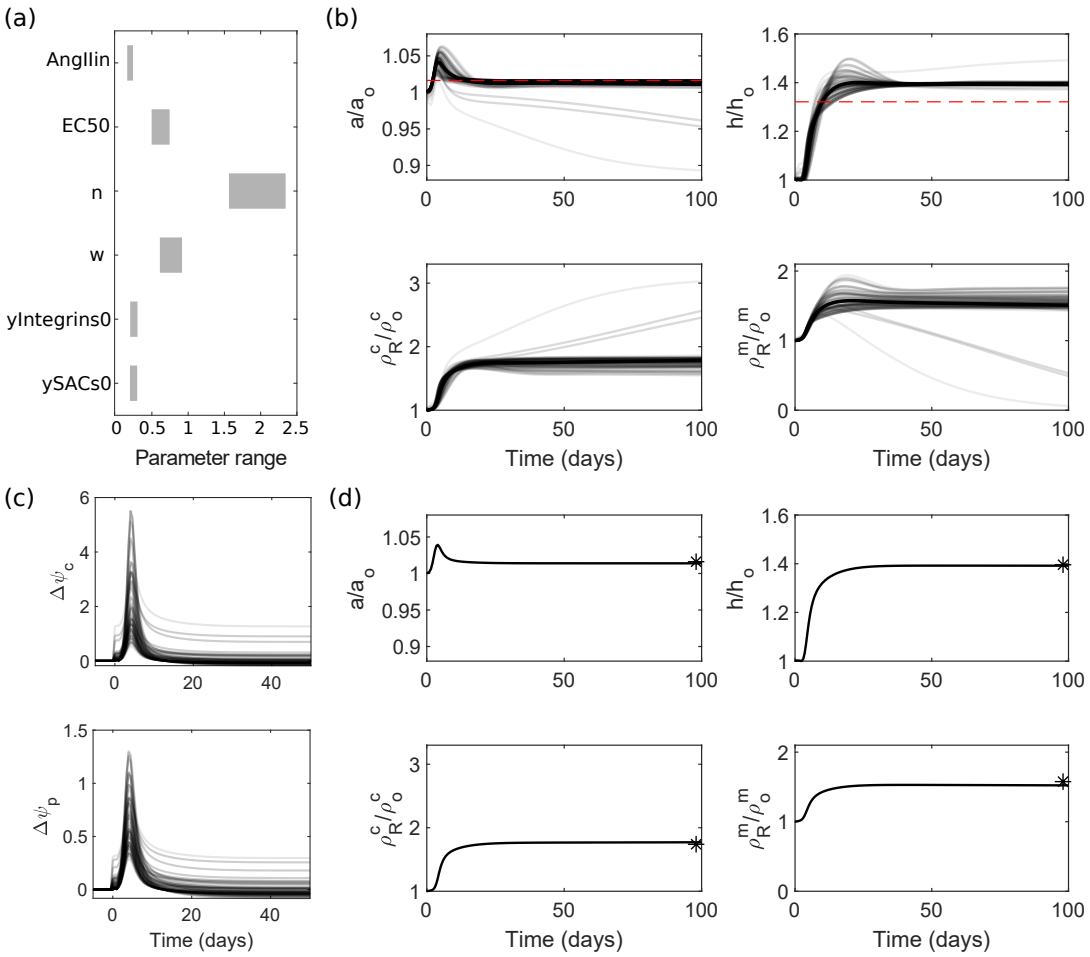

Figure 8: Sensitivity analysis of a single cell signaling network and a heterogeneous population of cells with collective behavior. (a) Parameter ranges, where parameters vary from their best-fit values by uniformly distributed noise of up to ±20% and (b) Overlayed timecourses for 30% pressure and 5% flow increases from homeostatic, where 100 parameter sets were sampled and applied to the network. We then apply these parameter sets to individual cells within a heterogeneous population, so that they respond collectively, and show (c) Overlayed collagen and intramural cell mass production stimuli, given by $\Delta\psi_c$ and $\Delta\psi_p$, respectively (Eqs 35, 48), for 100 cells that contribute to collective stimuli (Eq 52), and (d) Resulting timecourses for 30% pressure and 5% flow increases from homeostatic. Parameters vary by up to ±20% from baseline values: $y_{AngIIin}(0) = 0.20$, $y_{SACs}(0) = 0.248$, $y_{Integrins}(0) = 0.251$, $w = 0.763$, $n = 1.954$, and $EC_{50} = 0.621$. Additionally, $y_{Stress}(0) = 0.216$ and $y_{Wss}(0) = 0.436$. Asterisks in (d) indicate the values obtained under baseline conditions (no perturbations).

model predicted an unexpected natural history for tissue engineered vascular grafts used in congenital heart procedures, enabling a promising FDA-approved clinical trial to resume.[10] Notwithstanding the potential for both clinical impact and advancing basic understanding, given the continually increasing information available on transcriptional changes (*e.g.* bulk and single cell RNAseq) and associated cell signaling, there is a pressing need to incorporate such information into models that predict tissue-level clinical phenotypes.

This need for coupling tissue-level G&R and cell-level signaling models has been increasingly recognized, with recent developments reviewed.[25] Two general approaches at the signaling level are to use continuum descriptions by considering species concentrations and reaction kinetics in a system of differential equations, or to use discrete rule-based approaches such as agent-based models. For vascular remodeling, a reaction–diffusion partial differential equation system for three species (TGFβ, MMPs, and interleukins) has informed a tissue-level G&R model for a bilayered cylindrical vessel,[22] with several important microstructural features (collagen fiber diameter and crosslinking) influenced by these species; however, this influence is unidirectional, and molecular species do not depend on the mechanical state of the vessel. In a similarly motivated study, a system of ODEs was used (considering latent and active TGFβ, proteases, TIMPs, fibroblasts and inflammatory cells) to capture signaling related to aneurysm formation.[2] The signaling model was coupled to a tissue-level model for a bilayered cylindrical nonlinear elastic membrane, with TGFβ activity dependent on fibroblast stretch. Signaling outputs affected medial degradation, collagen growth, and fiber deposition stretches.

The more recently proposed logic-based approach[16] that we use has advantages of both discrete and continuum methods; starting from rule-based descriptions provides flexibility and intuition, whilst ODEs are efficient to simulate. We were confident that the current coupling could be achieved since the constrained mixture model has been coupled with an agent-based model[12] and, independently, an agent-based model has been coupled with a logic-based cell signaling model.[23] More recently, a logic-based model of cardiomyocyte signaling has been coupled to a fi-

nite element model of cardiac hypertrophy within a kinematic growth framework.[11] Nevertheless, this is to our knowledge the first coupling of models for logic-based cell signaling and constrained mixture-based tissue G&R. We verified the implementation, then validated the associated tissue-level predictions against experimental data for the murine infrarenal abdominal aorta and a broader class of arterial responses generated by a tissue-level G&R model that was validated against data from mouse models of hypertensive aortic remodeling,[19,21] though in the absence of inflammation. Given the central role of cell-driven matrix turnover, the mixture-level balance of mass relation is central to this coupling, and we thus focused on mass density production and removal. This relation also motivates evolving nonlinear, anisotropic mechanical properties of the wall via constituent-specific stored energy functions, thus facilitating the coupling further.

To challenge this new framework, we considered effects of perturbed signaling parameters. Tissue-level metrics of inner radius and wall thickness remained robust to uniformly distributed perturbations of up to $\pm 10\%$ (Fig 6), though this robustness was sometimes lost for $\pm 20\%$ (Fig 8(b)). To simulate cell heterogeneity, we modified the signaling model to consider 100 identical network structures, but with individually perturbed parameter sets. Individual stimuli were averaged to produce collective signaling behavior; in this case behaviors remained robust despite perturbations of up to $\pm 20\%$ (Fig 8(d)). This highlights one role of collective behavior and the protection it offers from the noise inherent to cell signaling networks. Note further that perturbations were uniformly distributed through a given range, but one might expect larger deviations to be admissable if relatively rare.

Although logic-based cell signaling models provide great flexibility in parameterization, we followed prior work on cardiac remodeling[29,26] wherein primary parameters (Hill parameter, n, EC_{50}, and reaction weight, w) were assumed uniform across the network. This simplification was evaluated by ensuring an overall coupled-fit to data; one particular sustained alteration in pressure and hemodynamics allowed the model to predict well multiple (fourteen) other alterations of interest. The advantage of this approach is the significant reduction in the number of parameters to

be identified, though with flexibility to refine parameters further to capture specific signaling if desired. Yet, any relaxation of this assumption requires additional data for intermediate signaling species; the model is not identifiable when using individual reaction parameters if only considering the six outputs used herein. Future refinements should thus be guided by additional cell-level data via western blots or single or bulk RNAseq, for which availability is rapidly increasing. Collection of both tissue- and cell-level data will additionally enable improved validation and refinement of the cell signaling component, which has so far only been compared qualitatively to results in the literature.[15] Other important future considerations include stress-driven cell apoptosis, which could be incorporated in the removal rate for cells, and active contraction of smooth muscle cells, where the contractility output (Fig 1) could be incorporated into an active stress contribution to the Cauchy stress. Finally, although we looked at parameter heterogeneity in identical networks (which demonstrates scalability of the approach), the same principles could support multiple different network structures (e.g. cell-specific signaling networks), or be used to investigate effects of perturbations in the network structure itself. This could accompany the use of more detailed tissue-level models, for example layer-specific signaling in a bilayered wall model.

Acknowledgments

This work was supported by grants from the US NIH (R01 HL105297, P01 HL134605, R01 HL139796, U01 HL142518, R01 HL146723).

References

[1] D. Ambrosi, M. Ben Amar, C. J. Cyron, A. DeSimone, A. Goriely, J. D. Humphrey, and E. Kuhl. Growth and remodelling of living tissues: perspectives, challenges and opportunities. *Journal of the Royal Society Interface*, 16 (157):20190233, 2019.

[2] P. Aparício, M. S. Thompson, and P. N. Watton. A novel chemo-mechano-

biological model of arterial tissue growth and remodelling. *Journal of Biomechanics*, 49(12):2321–2330, 2016.

[3] G. A. Ateshian and T. Ricken. Multigenerational interstitial growth of biological tissues. *Biomechanics and Modeling in Mechanobiology*, 9(6):689–702, 2010.

[4] C. Bellini, J. Ferruzzi, S. Roccabianca, E. S. Di Martino, and J. D. Humphrey. A microstructurally motivated model of arterial wall mechanics with mechanobiological implications. *Annals of Biomedical Engineering*, 42 (3):488–502, 2014.

[5] M. R. Bersi, C. Bellini, J. Wu, K. R. C. Montaniel, D. G. Harrison, and J. D. Humphrey. Excessive adventitial remodeling leads to early aortic maladaptation in angiotensin-induced hypertension. *Hypertension*, 67(5):890–896, 2016.

[6] M. R. Bersi, R. Khosravi, A. J. Wujciak, D. G. Harrison, and J. D. Humphrey. Differential cell-matrix mechanoadaptations and inflammation drive regional propensities to aortic fibrosis, aneurysm or dissection in hypertension. *Journal of The Royal Society Interface*, 14(136):20170327, 2017.

[7] L. Cardamone, A. Valentin, J. F. Eberth, and J. D. Humphrey. Origin of axial prestretch and residual stress in arteries. *Biomechanics and Modeling in Mechanobiology*, 8(6):431, 2009.

[8] C.-J. Chuong and Y.-C. Fung. Residual stress in arteries. In *Frontiers in Biomechanics*, pages 117–129. Springer, 1986.

[9] C. J. Cyron and J. D. Humphrey. Growth and remodeling of load-bearing biological soft tissues. *Meccanica*, 52(3):645–664, 2017.

[10] J. D Drews, V. K. Pepper, C. A. Best, J. M. Szafron, J. P. Cheatham, A. R. Yates, K. N. Hor, J. C. Zbinden, Y.-C. Chang, G. J. M. Mirhaidari, et al. Spontaneous reversal of stenosis in tissue-engineered vascular grafts. *Science Translational Medicine*, 12(537), 2020.

[11] A. C. Estrada, K. Yoshida, J. J. Saucerman, and J. W. Holmes. A multiscale model of cardiac concentric hypertrophy incorporating both mechanical and

hormonal drivers of growth. *Biomechanics and Modeling in Mechanobiology*, pages 1–15, 2020.

[12] H. N. Hayenga, B. C. Thorne, S. M. Peirce, and J. D. Humphrey. Ensuring congruency in multiscale modeling: towards linking agent based and continuum biomechanical models of arterial adaptation. *Annals of biomedical engineering*, 39(11):2669, 2011.

[13] J. D. Humphrey and K. R. Rajagopal. A constrained mixture model for growth and remodeling of soft tissues. *Mathematical Models and Methods in Applied Sciences*, 12(03):407–430, 2002.

[14] J. D. Humphrey, E. R. Dufresne, and M. A. Schwartz. Mechanotransduction and extracellular matrix homeostasis. *Nature Reviews Molecular Cell Biology*, 15(12):802–812, 2014.

[15] L. Irons and J. D. Humphrey. Cell signaling model for arterial mechanobiology. *PLoS Computational Biology*, 16(8):e1008161, 2020.

[16] M. J. Kraeutler, A. R. Soltis, and J. J. Saucerman. Modeling cardiac β-adrenergic signaling with normalized-Hill differential equations: comparison with a biochemical model. *BMC Systems Biology*, 4(1):157, 2010.

[17] E. Kuhl. Growing matter: a review of growth in living systems. *Journal of the Mechanical Behavior of Biomedical Materials*, 29:529–543, 2014.

[18] M. Latorre and J. D. Humphrey. A mechanobiologically equilibrated constrained mixture model for growth and remodeling of soft tissues. *ZAMM-Journal of Applied Mathematics and Mechanics/Zeitschrift für Angewandte Mathematik und Mechanik*, 98(12):2048–2071, 2018.

[19] M. Latorre and J. D. Humphrey. Modeling mechano-driven and immuno-mediated aortic maladaptation in hypertension. *Biomechanics and modeling in mechanobiology*, 17(5):1497–1511, 2018.

[20] M. Latorre and J. D. Humphrey. Fast, rate-independent, finite element implementation of a 3D constrained mixture model of soft tissue growth and

remodeling. *Computer Methods in Applied Mechanics and Engineering*, 368: 113156, 2020.

[21] M. Latorre, M. R. Bersi, and J. D. Humphrey. Computational modeling predicts immuno-mechanical mechanisms of maladaptive aortic remodeling in hypertension. *International Journal of Engineering Science*, 141:35–46, 2019.

[22] M. Marino, G. Pontrelli, G. Vairo, and P. Wriggers. A chemo-mechano-biological formulation for the effects of biochemical alterations on arterial mechanics: the role of molecular transport and multiscale tissue remodelling. *Journal of The Royal Society Interface*, 14(136):20170615, 2017.

[23] S. M. Rikard, T. L. Athey, A. Nelson, S. L. M. Christiansen, J.-J. Lee, J. W. Holmes, S. M. Peirce, and J. J. Saucerman. Multiscale coupling of an agent-based model of tissue fibrosis and a logic-based model of intracellular signaling. *Frontiers in physiology*, 10:1481, 2019.

[24] J. J. Saucerman, P. M. Tan, K. S. Buchholz, A. D. McCulloch, and J. H. Omens. Mechanical regulation of gene expression in cardiac myocytes and fibroblasts. *Nature Reviews Cardiology*, 16(6):361–378, 2019.

[25] V. D. Sree and A. B. Tepole. Computational systems mechanobiology of growth and remodeling: Integration of tissue mechanics and cell regulatory network dynamics. *Current Opinion in Biomedical Engineering*, 2020. doi: 10.1016/j.cobme.2020.01.002.

[26] P. M. Tan, K. S. Buchholz, J. H. Omens, A. D. McCulloch, and J. J. Saucerman. Predictive model identifies key network regulators of cardiomyocyte mechano-signaling. *PLoS Computational Biology*, 13(11):e1005854, 2017.

[27] A. Valentin and J. D. Humphrey. Evaluation of fundamental hypotheses underlying constrained mixture models of arterial growth and remodelling. *Philosophical Transactions of the Royal Society A: Mathematical, Physical and Engineering Sciences*, 367(1902):3585–3606, 2009.

[28] S. R. Van Doren. Matrix metalloproteinase interactions with collagen and elastin. *Matrix Biology*, 44:224–231, 2015.

608 [29] A. C. Zeigler, W. J. Richardson, J. W. Holmes, and J. J. Saucerman. A
609 computational model of cardiac fibroblast signaling predicts context-dependent
610 drivers of myofibroblast differentiation. *Journal of Molecular and Cellular Car-*
611 *diology*, 94:72–81, 2016.